

Abundant Organic Dye as an Anolyte for Aqueous Flow Battery with Multielectron Transfer

Alolika Mukhopadhyay,[†] Huijuan Zhao,[‡] Bin Li,^{§,⊥} Jonathan Hamel,[†] Yang Yang,[†] Daxian Cao,[†] Avi Natan,[†] and Hongli Zhu^{*,†}

[†]Department of Mechanical and Industrial Engineering, Northeastern University, 360 Huntington Avenue, Boston, Massachusetts 02115, United States

[‡]Mechanical Engineering Department, Clemson University, 201 Fluor Daniel EIB, Clemson, South Carolina 29634-0921, United States

[§]Electrochemical Materials and System Group, Pacific Northwest National Laboratory, 902 Battelle Boulevard, Richland, Washington 99352, United States

Supporting Information

ABSTRACT: Organic redox flow batteries have the potential to surpass the challenges posed by inorganic electrolytes commonly used in flow batteries, thus achieving high performance and a sophisticated storage solution for the grid. Herein, we demonstrated a high performance aqueous organic redox flow battery (AORFB) utilizing a redox-active resource from nature, indigo carmine (5,5'-indigodisulfonic acid sodium salt) (IC-Na), as the anolyte. The 5,5'-indigodisulfonic acid (IC-H) is obtained through the substitution of sodium ions in IC-Na with protons (H⁺). The aqueous solubility of IC-H was increased dramatically from 0.035 to 0.760 M (1.52 M electron concentration) in protic solvents. The diffusion coefficients (IC-Na, 1.06 × 10⁻⁵ cm² s⁻¹; IC-H, 2.19 × 10⁻⁵ cm² s⁻¹) and reaction rate constants (IC-Na, 1.93 × 10⁻⁴ cm s⁻¹; IC-H, 1.86 × 10⁻⁴ cm s⁻¹) of IC-Na and IC-H indicate rapid reaction kinetics. The highly soluble and affordable IC-H with fast redox kinetics was used as a sustainable anolyte by pairing with different catholytes. Moreover, a computational study was conducted which signifies the prospect of further improvements in solubility and voltage window by tuning the structure. Therefore, the environmentally benign and earth-abundant IC-H represents a promising choice for green and sustainable redox active anolyte of AORFB.

KEYWORDS: redox flow battery, blue dye, indigo carmine, sustainability, organic electrolyte



1. INTRODUCTION

The rapid growth of renewable energy sources such as wind and solar energy can supply a significant amount of electricity all over the world,¹ but their inherent intermittency and fluctuating nature are two of the essential barriers to utilizing this enormous amount of electricity available from renewable sources.² This intermittent nature of renewable sources led to an emerging need for efficient, cost-effective, and sustainable grid storage technologies. Redox flow batteries (RFBs) are particularly attractive and suitable for grid storage as they can scale power and energy independently.³ Although the RFBs have been recognized as a viable technology for reliable and extended duration grid-scale load deferment, the extensive utilization of the RFBs has been limited by the toxicity and lack of natural abundance of the inorganic electrolytes.⁴

To overcome these limitations encountered by the existing inorganic RFBs, researchers demonstrated several promising organic and organometallic electrolyte materials^{4–12} as they have the potential to surpass the challenges of inorganic flow batteries and lead to a sophisticated storage solution for the grid.¹³ For instance, anthraquinone and its derivatives have

been studied extensively for their rapid redox kinetics and chemical stability.^{7,8,14,15} Our previous study also utilized the redox chemistry of naturally occurring quinone, ultrafiltered lignin, to construct a low cost and earth-abundant electrolyte for AORFB.¹⁶ In addition to the acidic electrolytes, alloxazine² and phenazine¹⁷ based electrolytes in alkaline medium were also employed to develop AORFBs.

The redox activities of other organic molecules such as TEMPO (2,2,6,6-tetramethylpiperidine-1-oxyl),^{10,11} viologens,^{4,10,12,18} and ferrocene^{4,19,20} were investigated in neutral conditions to demonstrate high voltage and high-performance novel AORFBs. Despite the substantial advances in organic electrolytes, only a small number of AORFBs take advantage of organic redox active compounds for the electrolytes due to their low energy densities, poor stability, the high cost of the electrolytes, and lack of abundance in nature. Therefore, the key to reducing the capital cost and the environmental impact

Received: July 23, 2019

Accepted: September 26, 2019

Published: September 26, 2019

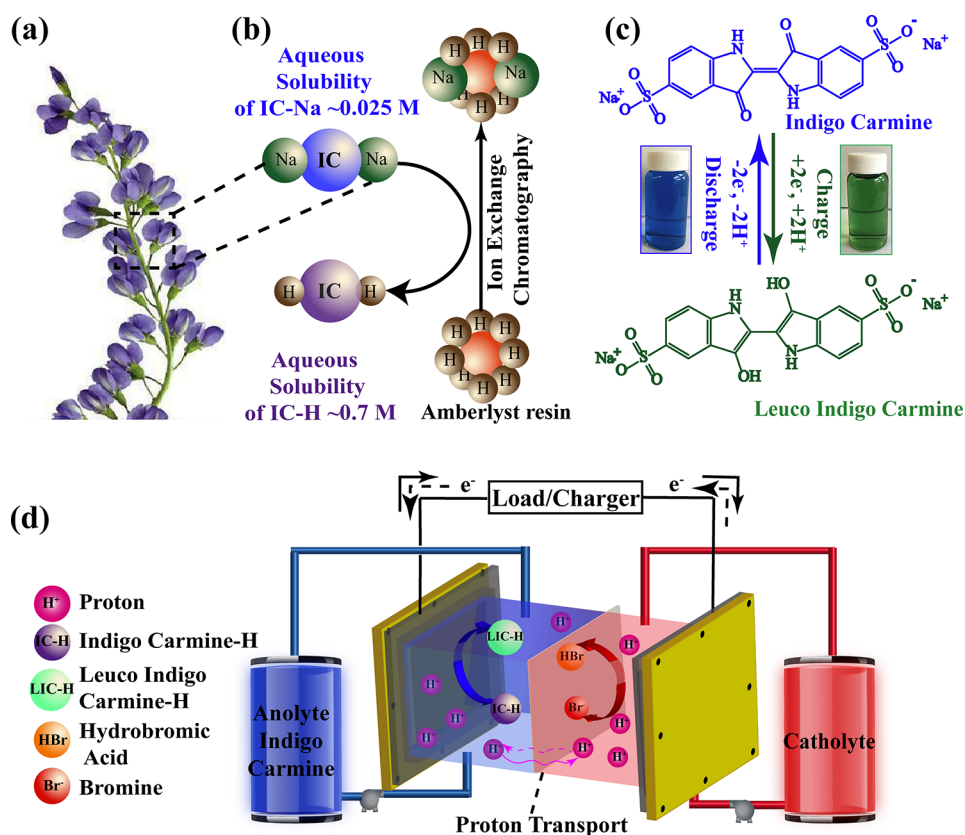


Figure 1. (a) Indigo fera plant from where the parent dye indigo can be extracted. (b) Schematic illustration of the ion exchange mechanism of IC-Na using amberlyst H resin. (c) Structural illustration of IC-Na participating in a redox reaction by accepting and releasing two electrons and two protons. (d) Schematic representation of the IC-H/Br₂ flow cell diagram.

of the AORFB is the utilization of abundant and ubiquitous natural resources to obtain a cost-effective and nontoxic electrolyte.

Herein, we introduce an earth-abundant and redox active natural polymer IC-Na (5,5'-indigodisulfonic acid sodium salt) from nature as a promising anolyte for AORFB to curtail the cost of the electrolytes, eliminate complicated synthesis processes, and simultaneously diminish the concern of availability for large-scale storage.²¹ Although the redox property of IC-Na has been studied before,²² the performance evaluation of IC-Na and IC-H in a flow cell has never been done. IC-Na, a water-soluble derivative of the naturally occurring indigo dye, has been used since ancient times for dyeing and printing²³ and can be obtained from more than 50 different species of plants.²⁴ Meanwhile, IC-Na is authorized for a wide range of food categories with maximum permitted levels between 50 and 500 mg kg⁻¹ of food,^{25,26} which identifies the benignity of IC-Na. Other favorable features of IC-Na include a highly rapid and reversible redox reaction, excellent stability, and structural modularity that are absolutely necessary for an anolyte of an AORFB.

However, the major challenge of using pristine IC-Na as an electrolyte directly in the flow battery is its poor aqueous solubility (10 g L⁻¹). A scalable ion-exchange process is performed to overcome this limitation by replacing the sodium ions with protons in the IC-Na²² that leads to a significant improvement (22-fold) in solubility (from 0.035 to 0.760 M in 0.1 M HClO₄), owing to the intermolecular hydrogen bond formation in protic solvents. With this high solubility, the obtained IC-H yields a volumetric capacity of 24.2 Ah L⁻¹ with

an energy density of 20.6 Wh L⁻¹ while paired with bromine/hydrobromic acid (Br₂/HBr) catholyte. The IC-H also achieves a round-trip energy efficiency of 77% and average capacity retention of 99.96% per cycle when paired with a Br₂/HBr catholyte. In addition, the IC-H obtained a capacity of 13 Ah L⁻¹ at 40 mA cm⁻² when paired with TEMPO. To further raise the solubility and voltage window, a high throughput computational study was also conducted to determine the optimum position and the type of the functional group that lowers the redox potential of the IC-Na and further increases the solubility.

2. RESULTS AND DISCUSSION

Figure 1a illustrates the natural source of the indigo dye. The most natural product from which indigo is obtained includes indican (genus *Indigofera* plants) and isatan (woad plants or *Isatis tinctoria*) in tropical and moderate climate zones, respectively.²⁷ Irrespective of their source, the chemistry of the dye extraction involves soaking the leaves of the plants in water to facilitate the fermentation process, during which the indican readily undergoes enzymatic hydrolysis and releases indoxyl that converts to indigo by oxidation upon exposure to air. IC-Na can be obtained from indigo by sulfonation, which renders the compound water-soluble by attaching two sulfonic acid groups to the indigo core.²⁸ However, sulfonating indigo to form IC-Na is not sufficient to obtain a high concentration of the electrolyte for the AORFB due to the extensive π stacking of IC-Na, which limits its application in AORFB. On the contrary, a high concentration of reactants in solution is the key to minimizing the storage tank size while obtaining

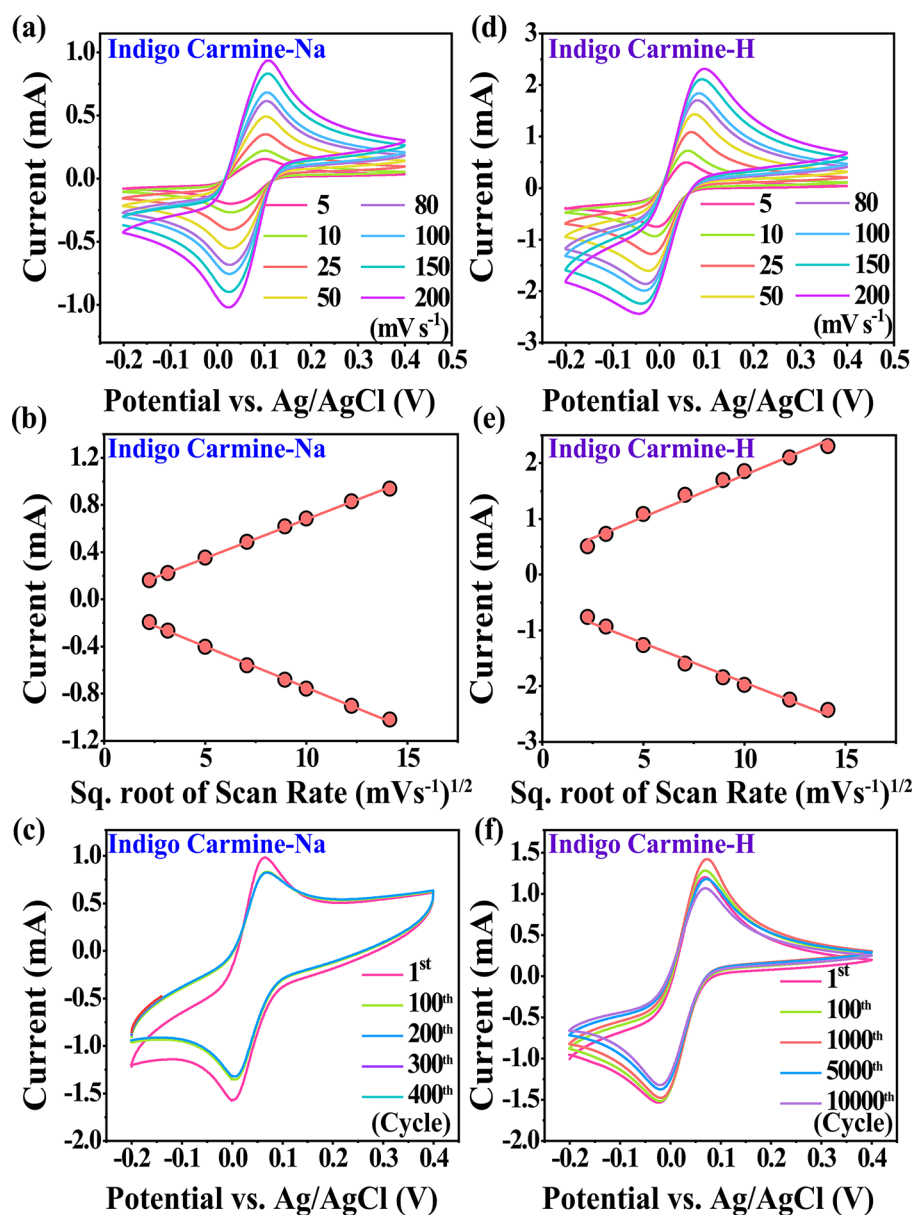


Figure 2. Electrochemical half-cell measurements of 10 mM IC-Na and IC-H in 0.1 M HClO_4 . (a) CV of IC-Na recorded between -0.2 and 0.4 V vs Ag/AgCl at scan rates from 5 mV s^{-1} to 200 mV s^{-1} . (b) Dependence of the redox peak currents on scan rates for IC-Na. (c) CV of IC-Na cycled for 500 times at 40 mV s^{-1} scan rate. (d) CV of IC-H recorded between -0.2 and 0.4 V vs Ag/AgCl at scan rates ranging from 5 mV s^{-1} to 200 mV s^{-1} . (e) Dependence of the redox peak currents on scan rates for IC-H. (f) CV of IC-H cycled 10 000 times at 40 mV s^{-1} scan rate.

high specific volumetric energy density. Therefore, the design of an appropriate electrolyte for AORFB starts from identifying redox-active materials followed by optimization of the structure to achieve the maximum solubility to maximize the energy density. In this study, in order to increase the solubility of IC-Na, it was converted to its acid analog (IC-H) by replacing the sodium ions in IC-Na with protons by passing through a column packed with amberlyst 15 hydrogen resins (Figure 1b).²² The conversion of IC-Na to IC-H was conducted on a large scale with more than 90% yield, and the solubility of the obtained IC-H is 0.76 M in 0.1 M HClO_4 owing to the intermolecular hydrogen bond formation. In IC-H, the substituted protons are attached to the strongly electronegative oxygen atoms and capable of forming strong hydrogen bondings. Hydrogen bondings are usually stronger than the van der Waals forces and dipole interactions. Thus,

the highly polar IC-H exhibits high intermolecular forces between the solute and the protic solvents and increases the solubility drastically. Figure 1c schematically illustrates the structure, redox mechanism of IC-Na with the release and accepting of two electrons and two protons, and appearance at different oxidation states in an acidic medium. IC-Na accommodates two-electron transfer leading to exceptional capacities. It undergoes a rapid and highly reversible reduction and oxidation to form leucoindigoid species (LIC-Na), which makes it suitable for its application as an anolyte in AORFB.²⁹ IC-Na contains a $\text{C}=\text{C}$ bridged structure with one six-membered and another five-membered aromatic ring on each side. IC-Na is a blue crystalline powder with a purplish luster due to the conjugation of the double bonds.^{30–32} In the molecular structure of organic crystal IC-Na, electron donor groups ($-\text{NH}$ and $-\text{OH}$) and electron acceptor group ($\text{C}=\text{C}$

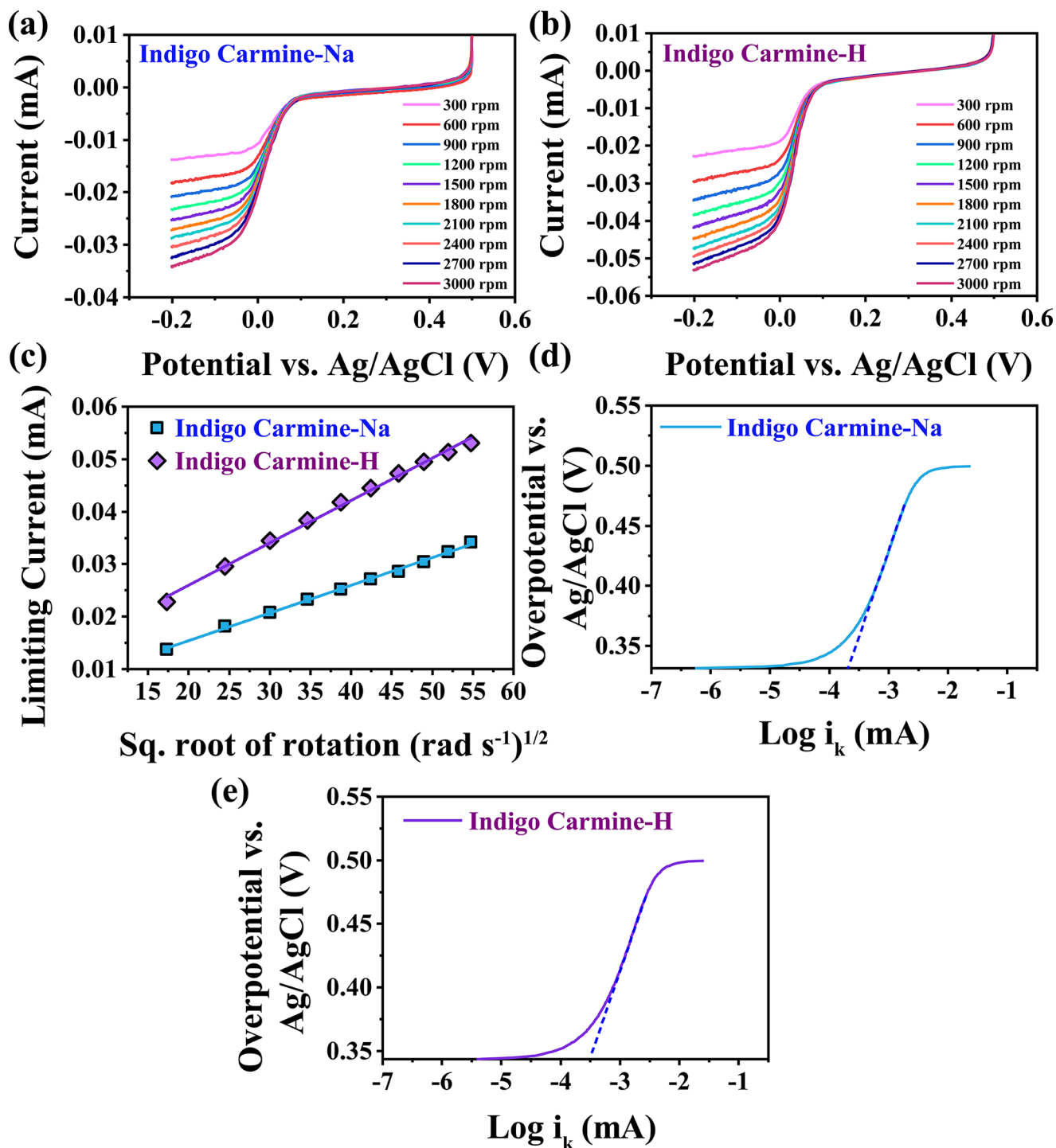


Figure 3. Rotating disk electrode measurements of 1 mM (a) IC-Na and (b) IC-H solutions in 0.1 M HClO₄ at different rotation speeds ranging from 300 to 3000 rpm with an increment of 300. (c) Levich plots (limiting current vs square root of rotation) of IC-Na and IC-H, which are derived from (a) and (b), respectively. The plots of overpotential versus the logarithm of kinetic current and the corresponding fitted Tafel plots for (d) IC-Na and (e) IC-H.

O) are attached by conjugated bonds, which are responsible for the dark blue shade of the IC-Na. In the reduced state, the dark blue color of the IC-Na changes to green, as shown in Figure 1c. To demonstrate the full cell performance of IC-H in the AORFB, we paired IC-H with Br₂/HBr, as depicted in Figure 1d. The IC-Na/Br₂ and IC-H/Br₂ batteries were assembled by stacking pretreated carbon paper electrodes at both sides separated by a Nafion proton exchange membrane,

and the solutions of IC-Na (0.035 M IC-Na in 0.1 M HClO₄) and IC-H (0.7 M IC-H in 0.2 M HClO₄) were pumped through the negative side, while the Br₂/HBr (0.5 M Br in 3.0 M HBr) was pumped through the positive side of the cells, respectively. In order to evaluate the performance of IC-Na and IC-H as anolytes of AORFB, an excess quantity of catholyte was used in the positive side to ensure that the anolyte stays on the capacity limiting side all the time.

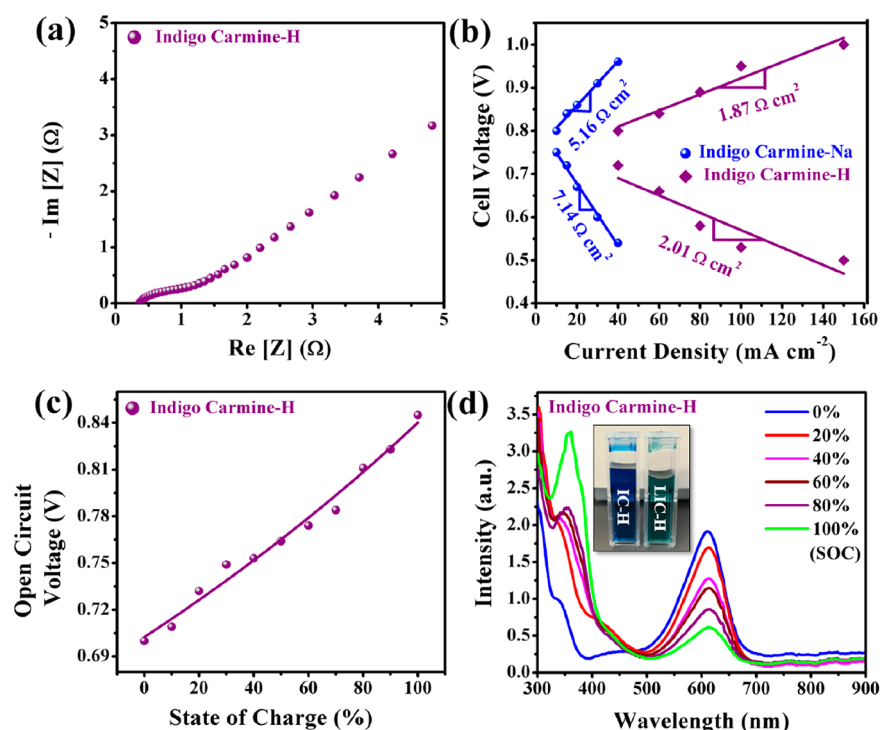


Figure 4. (a) Electrochemical impedance spectroscopy (EIS) of IC-H/Br₂ cell within a frequency range of 1 MHz to 10 mHz. (b) Cell voltage vs current density plot of IC-Na and IC-H cells when paired against Br₂/HBr. The polarization resistances were determined from the slope of the fitted curves of charge and discharge. (c) Variation in OCV of IC-H/Br₂ cell at a different SOC. (d) UV-vis spectra of IC-H at different SOC ranging from 0% to 100% during the charging process of the IC-H/Br₂ cell at 40 mA cm⁻² with an upper cutoff voltage of 1.4 V.

To achieve a better understanding of the redox reaction, electrochemical measurements in a half-cell were obtained for both IC-Na and IC-H. As illustrated in Figure 2a, cyclic voltammetry (CV) of IC-Na displays a pair of sharp and well-defined cathodic peak at ~ 0.0 V and anodic peak at ~ 0.035 V vs Ag/AgCl at varying scan rates with a peak separation of 0.035 V, which is close to the theoretically expected value of 0.0295 V (0.059 V/ n , n being 2 since two electrons are involved in the reaction), corresponding to the reversible reduction and oxidation of IC-Na to LIC-Na.³³ The conversion of the IC-Na to LIC-Na depends on the two-electron enolization process, where the two ketone groups containing IC-Na convert to two enol groups containing LIC-Na by two successive symmetric protonation processes.³⁴ Figure 2b demonstrates the dependence of the redox peak current for the reduction and oxidation on square root of the scan rate, which shows a linear behavior indicating a diffusion controlled process for IC-Na. In addition, the CV of IC-Na was also cycled 500 times, as shown in Figure 2c. It is worth mentioning that the reduced state of IC-Na (LIC-Na) is sensitive to oxygen and the solution was sparged with nitrogen before starting the experiment and sealed properly to avoid oxygen exposure. The obtained CV curves of 100th, 200th, 300th, 400th, and 500th cycles exactly overlap, which can be attributed to the excellent reversibility of the IC-Na due to its mesomeric structure and intramolecular hydrogen bonding. However, a shrinkage in peak size after the first cycle was observed and was attributed to the dissolved oxygen in the water.

The IC-H also displays a sharp pair of redox peaks centering around 0.05 V vs Ag/AgCl and separated by 40 mV at varying scan rates ranging from 5 mV s⁻¹ to 200 mV s⁻¹ (Figure 2d), which can be attributed to the rapid and reversible reduction

and oxidation of IC-H to the acid analog of leuco indigo carmine (LIC-H). The scan rate dependence of redox peaks for IC-H also displays a linear behavior (Figure 2e), similar to the IC-Na, indicating a diffusion-controlled process. However, compared to IC-Na (Figure 2b), IC-H generates higher current under the same scan rate. Further, the CV of IC-H was also evaluated in 3 M sulfuric acid, which exhibited a redox peak centering around 0.05 V (Figure S7).

In addition, the CV of IC-H was cycled 10 000 times at 40 mV s⁻¹ (as illustrated in Figure 2f) and a negligible decay observed after this extensive CV cycling that indicates high chemical stability attributable to the mesomer structure of the IC-H and its capability of forming hydrogen bonding. The structural analysis of indigo derivatives, conducted by Solís Correa et al. suggested the existence of two intramolecular hydrogen bonds between the adjacent ketone and the amine groups that inhabit the positions, which would otherwise be the most susceptible sites for nucleophilic and electrophilic attacks.³⁵ IC-H also exhibits intermolecular multicenter nonlinear hydrogen bonds between the amine and ketone groups of neighboring monomers protecting the indigo core again from the same reactive centers.³⁵ This extensive hydrogen bond formation and the steric hindrance confer stability to the structure by blocking the probable sites of nucleophile and electrophile attacks. Thus, the extremely stable structure, high reversibility of the redox reaction, and high aqueous solubility of IC-H make IC-H a promising candidate as anolyte for AORFB.

To gain further insights into the electrochemical kinetics, linear sweep voltammetry (LSV) of IC-Na and IC-H (Figure 3) was conducted by using the classic rotating disk electrode (RDE) technique, where the glassy carbon disk was rotated at a variety of speeds ranging from 300 to 3000 rpm with an

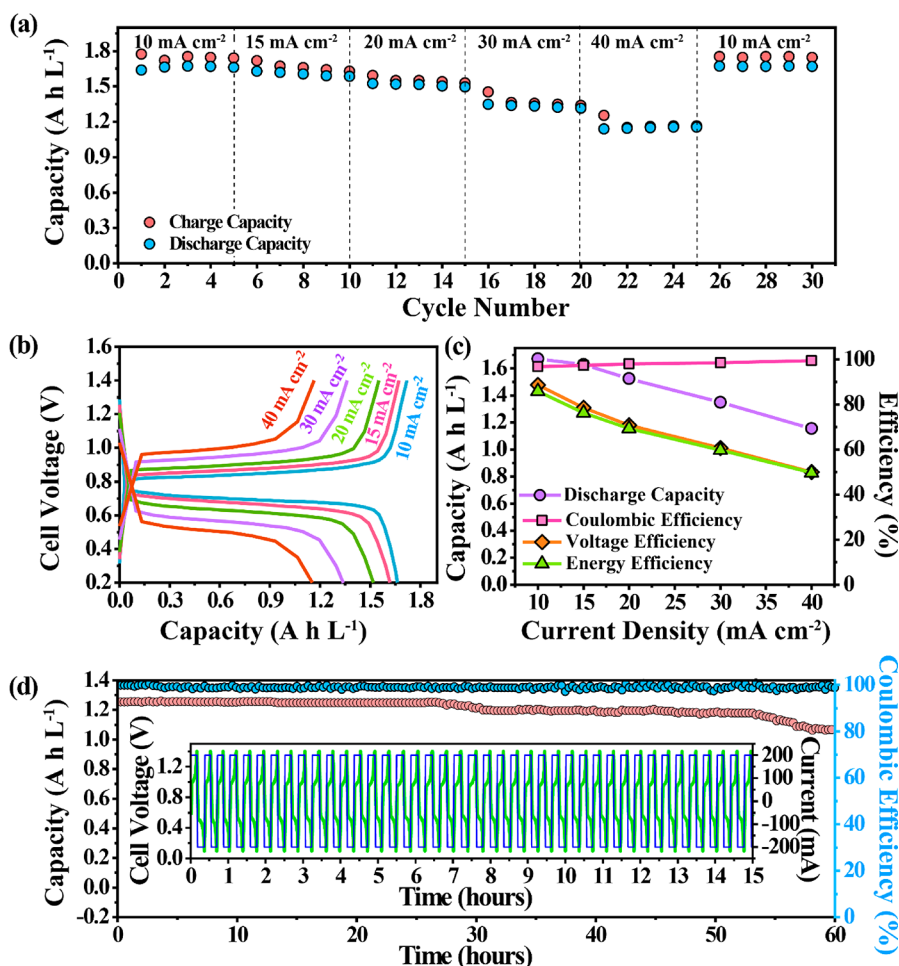


Figure 5. Demonstration of full cell performance of 0.035 M IC-Na in 0.1 M HClO₄ against 0.5 M Br₂ in 3 M HBr. (a) Cycle number versus capacity plot at various current densities. (b) Capacity versus cell voltage traces at different current densities. (c) Plots of averaged discharge capacity (purple circle), Coulombic efficiency (pink square), voltage efficiency (orange rhombus), energy efficiency (green sphere) versus current density of the IC-Na/Br₂ cell. (d) Constant current cycling of IC-Na/Br₂ cell at a current density of 40 mA cm⁻² with a cutoff voltage of 1.4 V during charge and 0.2 V during discharge.

increment of 300 rpm, and the LSV scans were performed at 25 mV s⁻¹ scan rate. The well-defined plateau observed at the LSV profiles of IC-Na and IC-H demonstrates the mass transport controlled limiting current, as depicted in Figure 3a and Figure 3b, respectively. Meanwhile, the LSV profiles of IC-H in 3 M H₂SO₄ were also determined as shown in Figure S7. The limiting current of IC-Na and IC-H exhibits a linear relationship with the square root of rotation (Figure 3c), which is in accordance with the Levich equation.¹⁰ The diffusion coefficients of the IC-Na and IC-H were calculated to be $\sim 1.06 \times 10^{-5}$ and 2.19×10^{-5} cm² s⁻¹, respectively, using the slope of the Levich plots (the detailed calculations are shown in the Experimental Section). The diffusion coefficients obtained for IC-Na and IC-H are higher^{16,36,37} or comparable¹⁰ to the other recently investigated organic electrolytes. Subsequently, to determine the rate constant of the charge transfer process, results of reduction overpotential of IC-Na and IC-H versus the logarithm of currents were plotted, as shown in Figure 3d and Figure 3e, respectively. The Tafel equation can be applied over 25 mV and 22 mV overpotential for the reduction of IC-Na and IC-H, respectively. In addition, the electron transfer rate constants of IC-Na and IC-H estimated from the fitted Tafel slopes (shown as the dashed line in Figure 3d and Figure 3e) are 1.93×10^{-4} and $1.86 \times$

10^{-4} cm s⁻¹, which are comparable to the recent organic species and most of the inorganic materials investigated for AORFB.^{15,36,38,39} Therefore, the fast mass transport and kinetic reduction rate constant obtained for the active species suggest a negligible voltage loss due to the rate of the electrochemical redox reaction at the surface of the electrode and ensure a high operational current density of the flow cell. Consequently, the obtained kinetic results further verify the feasibility of using IC-Na and IC-H as anolytes in AORFB.

Figure 4a is the measured Nyquist impedance spectrum at the open circuit of an IC-H/Br₂ flow cell in a static condition that shows a semicircle at the high-frequency region and a straight line at the low-frequency region. The X-intercept of 0.35 Ω in the high-frequency region of the curve represents the bulk resistance, which includes the solution resistance of the electrolyte, electrode resistance, contact resistance of each component, and the resistance contributed by the Nafion membrane. The semicircle of diameter ~ 0.6 Ω represents minimal charge transfer resistance at the high-frequency region, which is consistent with the fast charge transfer constants of IC-Na and Br₂. The linear part indicates the resistance due to the diffusion of the electrolytes through the porous electrodes at low frequency. The cell can also obtain very low ASR, as displayed in Figure 4b, as low as 1.87 Ω cm²

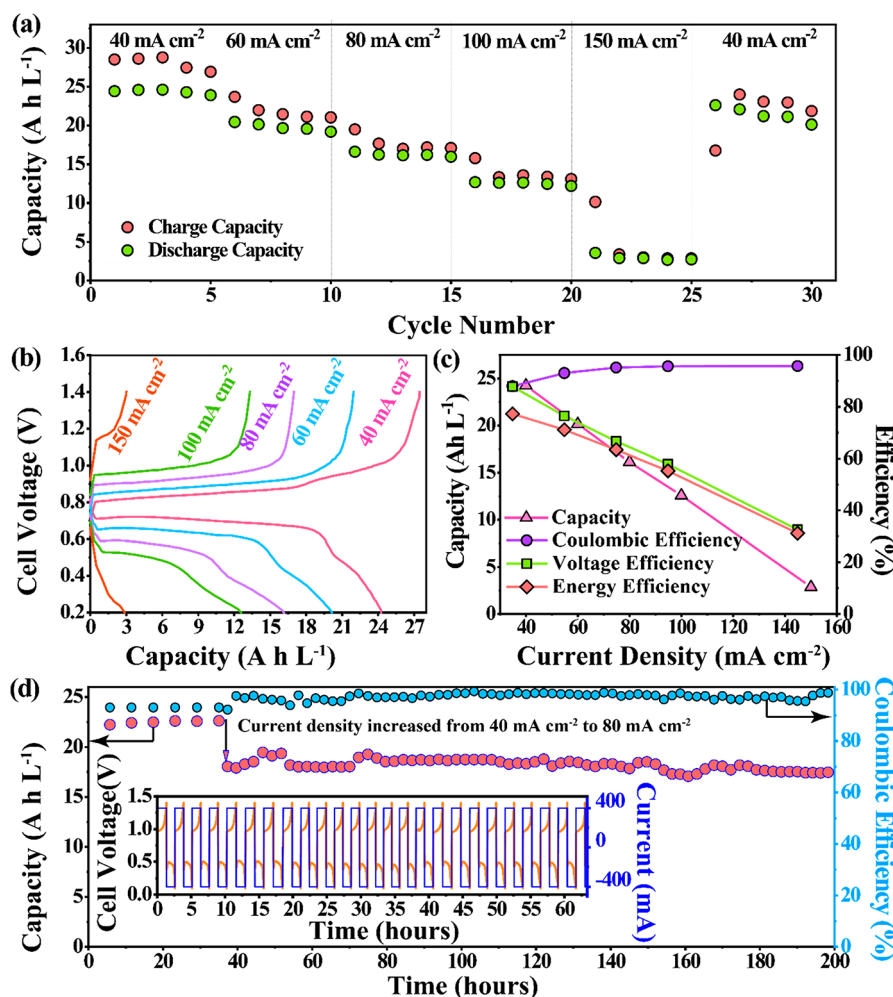


Figure 6. Demonstration of full cell performance of 0.7 M IC-H in 0.2 M HClO₄ against 0.5 M Br₂ in 3 M HBr. (a) Cycle number versus capacity plot at various current densities ranging from 40 mA cm⁻² to 150 mA cm⁻². (b) Capacity versus cell voltage traces at different current densities. (c) Plots of averaged discharge capacity (pink triangle), Coulombic efficiency (purple circle), voltage efficiency (green rectangle), energy efficiency (orange rhombus) versus current density of the IC-H/Br₂ cell. (d) Constant current cycling of IC-H/Br₂ cell at a current density of 20 mA cm⁻² with a cutoff voltage of 1.4 V during charge and 0.2 V during discharge.

on charge and 2.01 Ω cm² on discharge with excellent repeatability. The IC-H anolyte revealed an open circuit voltage (OCV) of 0.85 V when paired with Br₂/HBr, which is in good agreement with the predicted OCV of 0.89 V depending on the redox potential differences of Br₂/HBr (0.89 V vs Ag/AgCl) and IC-H (~0.05 V vs Ag/AgCl). The OCV of the full cell increased uniformly from 0.70 V at 0% state of charge (SOC) to 0.77 V at 50% SOC and 0.85 V at 100% SOC (Figure 4c), where the 0% and 100% SOC correspond to the fully discharged and charged states of the battery at a current density of 10 mA cm⁻². Further, to verify the reduction of the IC-H in the full cell, UV-vis absorption spectra of IC-H were recorded during the charging process of the cell at 40 mA cm⁻² current density, 1.4 V upper voltage cutoff, and at different SOC with wavelengths ranging from 300 to 900 nm (Figure 4d). At 0% SOC, the measured spectra of IC-H is in good accordance with the published spectra of IC-Na with two absorbance maxima at 335 and 610 nm within the wavelength range of 300–1000 nm, creditable to the indigo group present as the chromophore center.⁴⁰ However, during the charging process, the oxidized state (IC-H) and the reduced state (LIC-H) of the IC-H coexist in the electrolyte solution, which was verified by the fact that with increasing SOC, the

intensity of the peak at 335 nm increases, whereas the intensity of the other peak at 610 nm decreases linearly, indicating the increasing amount of LIC-H species in the anolyte. The color of the anolyte also changes from blue at 0% SOC to green at 100% SOC, as shown in the inset of Figure 4d. In addition, the color change of both of the active electrolytes further suggests the occurrence of the redox reactions at both sides and appropriate operation of the cell.

To gain further insight of the storage capability of IC-Na, the full cell tests were first performed using 0.035 M IC-Na in 0.1 M HClO₄ supporting electrolyte as negative electrolyte against 0.5 M Br₂ in 3 M HBr aqueous solution as a positive electrolyte and a Nafion proton exchange membrane. The current rate performance of the full cell, as shown in Figure 5a, was achieved by running the cell at six different current densities ranging from 10 mA cm⁻² to 40 mA cm⁻² for five consecutive times at each current density with a charge cutoff voltage of 1.4 V and a discharge cutoff voltage of 0.2 V, returning to the initial current density of 10 mA cm⁻², where it regains 100% of its original capacity. Lower current densities are chosen for IC-Na/Br₂ cell compared to the IC-H and other potential AORFB electrolytes due to the limited solubility of IC-Na (0.035 M in 0.1 M HClO₄).^{2,10,15,36} As presented in

Figure 5b, the IC-Na/Br₂ cell obtained discharge capacities of approximately 1.67, 1.63, 1.52, 1.35, and 1.15 Ah L⁻¹ at 10, 15, 20, 30, 40 mA cm⁻², respectively. Note that the discharge capacities were calculated considering the volume of the anolyte side. As anticipated, the increased voltage gaps observed in the charge–discharge plots exhibit the reduction in the achieved capacity with the increase in current density, which is a result of the increased ohmic loss and mass transport limitations at higher current densities. Moreover, the full cell has obtained Coulombic efficiencies of 96.78, 97.25, 97.96, 98.41, and 99.34%, voltage efficiencies of 88.65, 78.43, 70.79, 60.63, and 50%, and round-trip energy efficiencies of 85.79, 76.27, 69.34, 59.67, and 49.67% at current densities of 10, 15, 20, 30, and 40 mA cm⁻² (Figure 5c). Under similar conditions, the cell has also displayed a stable cycling performance for 200 successive cycles at 40 mA cm⁻², as demonstrated in Figure 5d. The average capacity retention of the cell is 99.91% per cycle (equivalent to an average capacity fade rate of 0.09% per cycle) even after 60 h (200 cycles) with a Coulombic efficiency of ~97% throughout the cycles. The average CE is slightly lower than 100% due to the crossover of bromine from catholyte side to the anolyte side.⁴¹ The decent capacity retention displayed by the IC-Na/Br₂ cell verifies the electrochemical stability of the IC-Na. It is also worth noting that the IC-Na can obtain an energy density of 2.24 W h L⁻¹ while paired with Br₂ with such a low concentration of 0.035 M, which can be further improved to 0.760 M by creating its acid analog. Therefore, it is evident that with proper optimization in structure, IC-Na can be a promising electrolyte for AORFB.

To demonstrate a high-performance AORFB, full cell performance of highly concentrated IC-H (0.7 M in 0.2 M HClO₄) was evaluated against Br₂/HBr (0.5 M Br₂ in 3 M HBr). The concentration of supporting electrolyte (HClO₄) was increased to 0.2 M for IC-H compared to the IC-Na since a higher concentration of IC-H was used. To obtain the rate performance of the IC-H/Br₂ cell, it was cycled at different current densities, five times at each current density, ranging from 40 mA cm⁻² to 150 mA cm⁻², and returned to the original current density of 40 mA cm⁻² as shown in Figure 6a. The IC-H exhibits excellent capacity retention with an average discharge capacity of 24.2, 20.1, 16.1, 12.6, and 2.9 Ah L⁻¹ at 40, 60, 80, 100, and 150 mA cm⁻², respectively, and regains 84% of its initial capacity when returned to the initial current density that indicates much-enhanced rate performance of IC-H at even higher current densities compared to the IC-Na due to the high concentration of the redox active molecules. However, it should be noted that the experiment lasted for more than 100 h and some visible Br₂ crossover was observed at the end of the experiment, which also explains the capacity fade. Crossover of Br₂ through the Nafion membranes is well-known. According to Li et al.⁴² crossover rate of Br₂ species through Nafion 212 membrane without an electric field is 0.11 mmol cm² h⁻¹, while the crossover rates are 0.3468 and 0.3858 mmol cm⁻² h⁻¹ for the charge and discharge processes, which are higher than the crossover rates without an electric field.

Further, Figure 6 b illustrates the typical charge–discharge profiles of IC-H/Br₂ cell at various current densities that exhibit a decrease in capacity at higher current densities owing to the increased ohmic loss, which is also consistent with the results obtained for IC-Na. The charge and discharge curves at each current density demonstrate two distinct plateaus, among which one is dominant and contributes to approximately 70–76% of the total capacity and the other one is weak and

delivers the remaining 30–24% of the capacity. The existence of two plateaus during charge is probably due to the two electron enolization process, where the two ketone groups containing IC-H converts to two enol groups containing LIC-H by two successive symmetric protonation processes. According to Moreno et al., the relative activation energy of one protonation process is more than 6 times higher than the other protonation process.³⁴ This significant difference in activation energy can cause different overpotential for the two successive protonation processes of IC-H, which is also consistent with the shoulder obtained in the previously published CV²² of IC-Na. We will follow up with a further systematic study regarding this phenomenon.

Compared to IC-Na, IC-H delivers much-enhanced discharge capacities at higher current densities leading to an energy density of 20.6 W h L⁻¹ with a corresponding power density of 48 mW cm⁻² at 40 mA cm⁻² and 13.7 W h L⁻¹ energy density with a corresponding power density of 96 mW cm⁻² at 80 mA cm⁻² at 100% SOC. Figure 6c shows the plot of discharge capacity, Coulombic efficiency, voltage efficiency, and the energy efficiency at different current densities. The voltage efficiency of the cell decreased from 88% at 40 mA cm⁻² to 58% at 100 mA cm⁻² and to 33% at 150 mA cm⁻², whereas the energy efficiency decreased from 77% at 40 mA cm⁻² to 55% at 100 mA cm⁻² and to 33% at 150 mA cm⁻². The cell exhibited Coulombic efficiencies of 88.0, 93.0, 95.1, 95.5, and 96.0% at current densities of 40, 60, 80, 100, and 150 mA cm⁻², respectively. The voltage efficiency and the energy efficiency of the cell followed the typical trend of decreasing with an increase in current density. However, the Coulombic efficiency exhibited a reverse trend of increasing with the increasing current density, which can be attributed to the increase in the discharge time at lower current densities. This reverse trend can be designated to the severe oxygen sensitivity of the reduced state of the IC-H which affects the overall Coulombic efficiency of the cell. Even though the electrolytes chambers were sparged with nitrogen and sealed properly to prevent any oxygen exposure, it was not possible to annihilate oxygen from the system with the dynamic flow cell setup and the longer cycling time at low current density. However, this problem can be easily solved by running the cell in an inert environment. The effect of oxygen is more predominant with the increase in the discharge duration.

To further validate the stability of IC-H, the cell was cycled for 35 h at a low current density of 40 mA cm⁻² and 165 h at a high current density of 80 mA cm⁻² continuously and retained 96.83% of its initial capacity, as displayed in Figure 6d. The average capacity retention of the cell is 99.54% per day, which is also identical to 99.96% capacity retention in each cycle, even after 200 h with an average Coulombic, voltage, and energy efficiencies of ~96, 67, and 64% for high current density cycling at 80 mA cm⁻² and 93, 88, and 77% for the low current density cycling at 40 mA cm⁻², respectively. More importantly, the capacity retention rate per cycle is comparable to the recently reported AORFBs such as 1,1-bis(3-sulfonatopropyl)-4,4-bipyridinium, (SPr)₂V/KI cell (99.99% per cycle) reported by Debruler et al.,⁴³ alkaline-soluble alloxazine 7/8-carboxylic acid RFB (99.98% per cycle) reported by Lin et al.,² (ferrocenylmethyl)trimethylammonium chloride/methyl viologen RFB reported by Hu et al.,⁴⁴ *p*-conjugation extended viologen, and 4,4'-(thiazolo[5,4-*d*]-thiazole-2,5-diyl)bis(1-(3-(trimethylammonio)propyl)pyridin-1-ium)tetrachloride [(NPr)₂TTz]Cl₄/4-trimethylammonium-

TEMPO (N^{Mc} -TEMPO) cell (99.97% per cycle) reported by Luo et al.,⁴⁵ among others. The inset of Figure 6 d exhibits the current and voltage profiles against time for 25 cycles at 80 mA cm^{-2} current density. This outstanding stability of IC-H is attributable to the excellent structural stability arising from the inter/intramolecular hydrogen bonding and negligible crossover of the IC-H due to its anionic nature and large molecular size. Overall, the outstanding stability, efficiencies, energy, and power densities achieved for the novel, low cost, and environmental friendly IC-H provide a promising direction for sustainable, cost-effective AORFB.

A current challenge for AORFB is to achieve a high energy density while minimizing the electrolyte cost, and the developed design meets both of these requirements. However, using Br_2 as a catholyte raises serious safety concern due to the high toxicity of Br_2 . Therefore, we have also paired IC-Na and IC-H with an organic TEMPO in 0.1 M $HClO_4$, which exhibits a pair of redox peaks around 0.75 V vs Ag/AgCl leading to a full cell OCV of 0.75 V. The full cell tests of IC-Na/TEMPO (0.035 M IC-H in 0.1 M $HClO_4$) and IC-H/TEMPO (0.7 M IC-H in 0.1 M $HClO_4$) have also achieved very high capacities with excellent capacity retention, as illustrated in Supporting Information Figures S2 and S3, respectively. However, the cell achieved much lower Coulombic efficiencies than the IC-Na/ Br_2 and IC-H/ Br_2 cell, as the cell suffered from the high crossover rate of radical cation TEMPO through the cation exchange Nafion membrane.

More improvements in the cell design can be made by further improving the solubility of IC-Na, decreasing the redox potential of IC-Na, or changing the pH of the supporting electrolyte. Organic molecules allow optimization of the critical criteria needed for the flow battery such as achieving higher solubility by introducing the solubilizing group, different redox potential to increase the voltage window by tuning the electron donating properties of the functional groups and decreasing crossover by changing the size or net charge. These optimizations can easily be done by chemically modifying the molecules, which can further be enhanced by a prior computational study to predict the solubility and redox potential.

Therefore, to better understand the additive effect of various functional groups on the indigo backbone, a detailed computational study was performed using density functional theory (DFT) calculations. Different electron donating groups such as hydroxyl ($-OH$), methyl ($-CH_3$), methoxy ($-OCH_3$) and electron withdrawing groups such as carboxyl ($-COOH$) and sulfonic acid ($-HSO_3$) were selected to study the additive effect on the solubilities and redox potentials of the IC-Na derivatives. Shown in Figure 7a, the electrostatic potential map of IC-Na indicates that the electron density in the IC-Na is mostly localized in the oxygen atoms of the ketone groups, while the most electron deficient regions are the H atoms of the phenyl and pyridine rings, thus making them more susceptible to the nucleophile attacks. Therefore, computations were carried out by inspecting all the possible substitutions for each functional group at every possible site of the IC-Na. Thirty molecules with different substitutions were screened. Selected results together with the substitution pattern of potential anolyte candidates are listed in Table 1, and a detailed table including the entire results of the analysis is presented in Supporting Information Table 1. Figure 7b shows the variation in predicted standard redox potential with the introduction of different functional groups to the backbone of

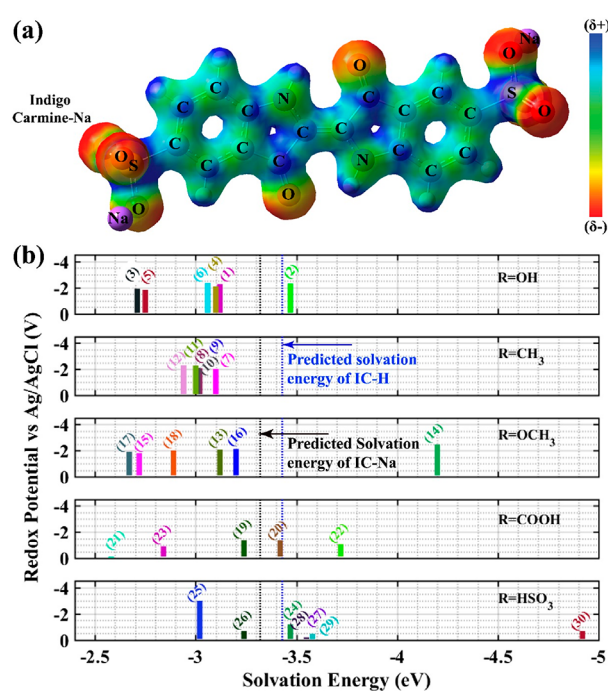
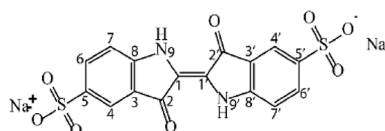


Figure 7. (a) Electrostatic potential map of IC-Na. (b) The plot of predicted redox potential vs solvation energy after addition of different functional groups such as electron donating groups (1–18) hydroxyl (1–6), methyl (7–12), and methoxy (13–18) and electron withdrawing groups (19–30) carboxyl (19–23) and sulfonate (24–30). The black and blue dotted line represents the solvation energy of pristine IC-Na without any substitution and hydrogen substituted IC-H, respectively. The numbering corresponds to the substitution patterns shown in Table 1 in the Supporting Information.

indigo. Addition of electron donating groups reduced the reduction potential drastically. Addition of hydroxyl, methyl, and methoxy lowered the redox potential drastically reaching up to -2.49 V vs Ag/AgCl, as shown in Figure 7b. Unexpectedly, the addition of electron withdrawing groups such as sulfonate and carboxyl lowered the cell potential for some configuration (Figure 7b). Similar results were also observed by Hollas et al.¹⁷ Moreover, the predicted redox potentials are in neutral medium (pH 7) and can be corrected for the strong acidic medium of pH 1 using the Nernst equation (equation S2 in Supporting Information). In addition, solvation energies of some of the derivatives are also higher than the solvation energy of IC-Na and IC-H (as represented in Table 1), indicating an improvement in the solubility. Therefore, the obtained computational results would be beneficial as an initial guideline for the selection of most promising candidates for AORFB anolyte among the various indigo derivatives. The selected anolyte candidates should (1) have solvation energy lower than IC-Na (<-3.32 eV, on the right of the black dotted line in Figure 7b) and (2) have a suitable redox potential depending on the potential of the catholyte to maintain the operational cell voltage within the water splitting voltage window, which is thermodynamically 1.23 V^{46,47} at standard conditions. Synthesizing the proposed molecules is beyond the scope of this work, but our future goal will be to synthesize the promising indigo derivatives, verify the theoretical predictions, and evaluate their performance in the full cell against various catholytes.

Table 1. Substitution Pattern and Predicted Redox Potential



index no.	functional group	position			solvation energy (eV)	redox potential (E_0 (V) vs Ag/AgCl)
		4,4'	5,5'	7,7'		
indigo carmine Na	no substitution				-3.32	-0.4
indigo carmine H	no substitution				-3.43	-0.42
2	R = OH	1 substituent				
		H	R	H	-3.47	-2.32
14	R = OCH ₃	1 substituent				
		H	R	H	-4.2	-2.49
20	R = COOH	1 substituent				
		H	R	H	-3.42	-1.37
22		2 substituents				
		R	R	H	-3.72	-1.07
24	R = HSO ₃	1 substituent				
		R	H	H	-3.47	-1.21
27		2 substituents				
		R	R	H	-3.58	-0.48
28		R	H	R	-3.55	-0.22
29		H	R	R	-3.58	-0.48
30		3 substituents				
		R	R	R	-4.92	-0.68

3. CONCLUSIONS

We demonstrated a novel AORFB with a sustainable and low-cost organic dye that can be extracted from naturally abundant plants readily following scalable and inexpensive method with a 90% yield. The extracted parent dye indigo can easily be modified by an ion exchange chromatography using amberlysts 15 hydrogen resin to create its acid analog, which increases the solubility from 0.035 to 0.76 M in 0.2 M HClO₄. In addition, IC-Na exhibits a reversible redox peak at 0 V vs Ag/AgCl in 0.1 M HClO₄ with rapid reaction kinetics. Pairing the acid analog of IC-Na with Br₂/HBr enables a voltage window of 0.85 and an energy density of 20.6 W h L⁻¹ with a corresponding power density of 48 mW cm⁻² at 40 mA cm⁻² current density. The full cell delivered an outstanding performance with an average round-trip energy efficiency of 77% at 40 mA cm⁻² current density. Further, the average capacity retention of each charge/discharge cycle was 99.54% per day. Moreover, tuning the structure of IC-Na can further enhance the aqueous solubility and boost the accessible capacity by increasing the voltage window. It is established that this approach of using naturally occurring organic dye as the active material for the flow battery can provide a low-cost and sustainable solution for distributed energy storage.

4. EXPERIMENTAL SECTION

4.1. Materials and Synthesis. To obtain the IC-H from IC-Na (Fisher Scientific, USA), an ion-exchange column was filled with Amberlyst 15 hydrogen resin (Fisher Scientific, USA) to ~6 in. height and preconditioned by passing 250 mL of 0.1 M H₂SO₄ solution. Then the column was washed with DI water until the pH of the outgoing solution from the column is 7. After the conditioning step, 1 g of IC-Na dissolved in 100 mL of DI water was flushed through the column to convert the IC-Na to its acid equivalent IC-H. The whole process was repeated three times. Then, the solvent was removed under controlled humidity, and the solid collected was dried under a vacuum at 70 °C for 48 h.

4.2. Three Electrode Electrochemical Characterization.

Cyclic voltammetry experiments were performed using a Biologic SP150 potentiostat controlled by Biologic EC-Lab software. All linear sweep voltammetry (LSV) studies were conducted using a Biologic SP150 potentiostat in a three-electrode setup. A 3 mm diameter Teflon encased glassy carbon disk working electrode (Pine Research Instrumentation) was rotated from 300 to 2700 rpm using a Pine MSR rotator system. A platinum foil counter electrode, an Ag/AgCl reference electrode, and Pine Instruments glassware were used for all the RDE studies. Before each experiment, the glassy carbon working electrode was polished on 600 grit paper to a mirror shine using 0.05 μm alumina suspension (Allied High Tech Products), sonicated for 10 min in ethanol, followed by a 10 min sonication in DI water. All LSV scans were logged at a rate of 5 mV s⁻¹, and to eliminate experimental error, each experiment was repeated three times. The limiting currents (i.e., the diffusion-limited current intensity) were measured at -0.2 V versus Ag/AgCl and plotted over the square root of the rotation rate (rad/s). The resulting plots were fitted to yield a straight Levich plot, where the slope defines the Levich equation, as presented in eq 1.

$$\text{slope} = 0.620nFAC_0D^{2/3}\nu^{-1/6} \quad (1)$$

where n is the number of electrons involved in the reaction that is 2 for this case, Faraday's constant $F = 96485 \text{ C mol}^{-1}$, electrode area $A = 0.1963 \text{ cm}^2$, indigo carmine's concentration $C_0 = 1.0 \times 10^{-3} \text{ M}$, kinematic viscosity $\nu = 0.0089 \text{ cm}^2 \text{ s}^{-1}$ for 0.1 M perchloric acid solution, and D is the diffusion coefficient.

The calculations yielded the diffusion coefficients of IC-Na and IC-H as 1.06×10^{-5} and $2.19 \times 10^{-5} \text{ cm}^2 \text{ s}^{-1}$, respectively. A plot of overpotential versus $\log_{10}(i_k)$ (i_k indicates the kinetic current for the reduction of IC-Na and IC-H) was built for the LSV data obtained at 2700 rpm and the X-intercepts of the fitted Tafel plots imply the logarithm of the exchange current i_0 . Further, the $\log(i_0)$ can also be represented as FAC_0k_0 , where k_0 is the electron transfer rate constant. From the above relation, using the obtained data, k_0 was calculated to be 1.93×10^{-4} for IC-Na and $1.86 \times 10^{-4} \text{ cm}^2 \text{ s}^{-1}$ for IC-H.

4.3. Flow Cell Electrochemical Characterization. The flow battery system consisted of a single battery cell assembly, two electrolyte tanks, peristaltic pumps for electrolyte circulation,

temperature control equipment, and pressure monitoring equipment. According to the previously published protocol,^{16,48} the cell was assembled using two gold-plated aluminum current collectors, two machined graphite plates with integrated column flow field, and silicon gaskets. The assembly was held together by eight 10-32 socket head screws torqued to 25 in. lbs. During assembly, six carbon papers (Sigracet 39AA, 280 μm thick, 80% porosity) were stacked at each side, and a Nafion 115 membrane (Chemours) was used as a separator. Carbon papers were pretreated by first sonicating in IPA for 5 min and soaking them into a 1:1 concentrated H_2SO_4 and HNO_3 mixture at 50 $^\circ\text{C}$ for 5 h. The carbon papers were triple rinsed with DI water before use. The membrane pretreatment method involved a 12 h soak in 0.1 M perchloric acid at room temperature, followed by triple rinsing in DI water prior to loading in the cell. The cell active area was 5 cm^2 , and an amount of 25 mL of electrolytes was used on both sides for testing the cell.

Electrochemical impedance spectroscopy (EIS) was performed by applying a sine voltage waveform of amplitude 10 mV added to an offset voltage. The frequency of the sine voltage was varied stepwise from 1 MHz to 10 mHz, with 10 points per decade in logarithmic spacing. The horizontal intercept of the Nyquist plot (a real component of the impedance) at the point where the imaginary component of the impedance was zero was multiplied by the geometric electrode area (5 cm^2) to obtain the high-frequency ASR.

4.4. State of Charge (SOC) Determination. The flow cell was charged at 10 mA cm^{-2} , and 500 μL of anolyte was taken out from the anolyte tank during the charging process at certain time intervals. The completely discharged cell was considered as 0% SOC, and completely charged cell was considered to be at 100% SOC. The samples were subjected to a 100-fold dilution, and a 2 mL aliquot was taken from this dilution. The spectroscopic measurements were performed with an Agilent 8453 UV–vis spectrometer (10 mm path length and quartz cuvette) at 1 nm intervals over the wavelength ranging from 300 to 1000 nm.

4.5. Viscosity Measurement. Viscosity testing was performed on candidate solution of 0.7 M at 2 and 5 s^{-1} shear rate within a temperature range of 25–40 $^\circ\text{C}$ using a Discovery HR-2 rheometer (TA Instruments, USA).

4.6. Conductivity and pH Test. Conductivity and pH measurements were taken using an Oakton pH/CON portable meter (PC 450). Calibration was done at room temperature using Oakton 1413 and 12880 μS conductivity standards (WD-00653-18, WD-00606-10) and Oakton 4 and 7 pH buffers (EW-00654-00, EW-00654-04).

4.7. Theoretical Calculations. The initial conformation of IC was created using Gauss View 5, and the geometries were optimized to a minimum energy level using DFT calculations in Gaussian 09. The geometry optimization and the single point frequency calculations were performed using B3LYP with split valence double- ζ (6-31G) or triple- ζ (6-311G) basis sets with polarization functions “(d,p)” that enhance the chemical structure by adding flexibility to atoms in forming chemical bonds in any direction and the diffuse functions “+” and “++” that improve the predicted properties with extended electronic densities.⁴⁹ We obtained the lowest error in the predicted redox potential of IC compared to the experimental using the basis set B3LYP/6-311G(d,p) (Table S2), and further calculations were done using the same basis set, as presented in Figure 7. The free energies of solvation were calculated using the conductor-like polarizable continuum model (overlapping sphere) with water as a solvent following eq S1 in the Supporting Information. Although acidic supporting electrolyte was used in this work, the solvent used for the prediction was water due to lack of details of dielectric properties of 0.2 M perchloric acid.¹⁷ In addition, it can be justified that the same assumption was made for all the compounds. Therefore, the predicted results could still reflect the solubility trend of the compounds relative to each other. To compare the changes in thermochemistry from the gas phase to aqueous solution, all the energetics related to solvation were analyzed in terms of the Gibbs free energies. The shift from pH 7 to pH 1 was estimated combining the experimental and predicted redox potential and Nernst equation, as represented in eq S2 in the Supporting Information, which is ~ 354

mV. Theoretical reduction potentials for the two-electron two-proton reaction were obtained from the Gibbs free energy difference between the dianion and the neutral forms of indigo carmine.

■ ASSOCIATED CONTENT

📄 Supporting Information

The Supporting Information is available free of charge on the ACS Publications website at DOI: 10.1021/acsaeem.9b01429.

The Viscosity of indigo carmine-H test, cell performance of indigo carmine-Na and indigo carmine-H vs TEMPO, table for substitution pattern and predicted redox potential for DFT calculation, hydrogen bonding schematic, TGA analysis, and half cell measurement of indigo carmine-H in sulfuric acid (PDF)

■ AUTHOR INFORMATION

Corresponding Author

*E-mail: h.zhu@neu.edu.

ORCID

Alolika Mukhopadhyay: 0000-0003-2085-7063

Hongli Zhu: 0000-0003-1733-4333

Present Address

¹B.L.: Energy and Environment Science and Technology, Idaho National Laboratory, 1955 North Fremont Avenue, Idaho Falls, Idaho 83415, United States

Author Contributions

H. Zhu supervised and conceived this project. A. Mukhopadhyay conducted the experiments, collected and analyzed data, and wrote the manuscript. H. Zhao and H. Zhu supervised the numerical modeling. J. Hamel and D. Cao contributed to the manuscript editing. B. Li gave suggestions for the flow cell tests. All the authors commented on the manuscript.

Notes

The authors declare no competing financial interest.

■ ACKNOWLEDGMENTS

This research was financially supported by a start-up and seed grant Tier 1 to H. Zhu from Northeastern University. We acknowledge the Center of Information Technology Services—Research Computing in Northeastern for providing access to Gaussian 09. We acknowledge the Kostas Nanomanufacturing Research Center for sharing the XRD.

■ REFERENCES

- (1) Wei, X.; Pan, W.; Duan, W.; Hollas, A.; Yang, Z.; Li, B.; Nie, Z.; Liu, J.; Reed, D.; Wang, W.; Sprenkle, V. Materials and systems for organic redox flow batteries: status and challenges. *ACS Energy Letters* **2017**, *2* (9), 2187–2204.
- (2) Lin, K.; Gómez-Bombarelli, R.; Beh, E. S.; Tong, L.; Chen, Q.; Valle, A.; Aspuru-Guzik, A.; Aziz, M. J.; Gordon, R. G. A redox-flow battery with an alloxazine-based organic electrolyte. *Nature Energy* **2016**, *1*, 16102.
- (3) Milshtein, J. D.; Barton, J. L.; Carney, T. J.; Kowalski, J. A.; Darling, R. M.; Brushett, F. R. Towards Low Resistance Nonaqueous Redox Flow Batteries. *J. Electrochem. Soc.* **2017**, *164* (12), A2487–A2499.
- (4) Beh, E. S.; De Porcellinis, D.; Gracia, R. L.; Xia, K. T.; Gordon, R. G.; Aziz, M. J. A neutral pH aqueous organic–organometallic redox flow battery with extremely high capacity retention. *ACS Energy Letters* **2017**, *2* (3), 639–644.

- (5) Mukhopadhyay, A.; Hamel, J.; Katahira, R.; Zhu, H. Metal-Free Aqueous Flow Battery with Novel Ultrafiltered Lignin as Electrolyte. *ACS Sustainable Chem. Eng.* **2018**, *6* (4), 5394–5400.
- (6) Gerhardt, M. R.; Tong, L.; Gómez-Bombarelli, R.; Chen, Q.; Marshak, M. P.; Galvin, C. J.; Aspuru-Guzik, A.; Gordon, R. G.; Aziz, M. J. Anthraquinone derivatives in aqueous flow batteries. *Adv. Energy Mater.* **2017**, *7* (8), 1601488.
- (7) Lin, K.; Chen, Q.; Gerhardt, M. R.; Tong, L.; Kim, S. B.; Eisenach, L.; Valle, A. W.; Hardee, D.; Gordon, R. G.; Aziz, M. J.; Marshak, M. P. Alkaline quinone flow battery. *Science* **2015**, *349* (6255), 1529–1532.
- (8) Wang, W.; Xu, W.; Cosimbescu, L.; Choi, D.; Li, L.; Yang, Z. Anthraquinone with tailored structure for a nonaqueous metal–organic redox flow battery. *Chem. Commun.* **2012**, *48* (53), 6669–6671.
- (9) Yang, B.; Hooper-Burkhardt, L.; Krishnamoorthy, S.; Murali, A.; Prakash, G. S.; Narayanan, S. High-performance aqueous organic flow battery with quinone-based redox couples at both electrodes. *J. Electrochem. Soc.* **2016**, *163* (7), A1442–A1449.
- (10) Liu, T.; Wei, X.; Nie, Z.; Sprenkle, V.; Wang, W. A total organic aqueous redox flow battery employing a low cost and sustainable methyl viologen anolyte and 4-HO-TEMPO catholyte. *Adv. Energy Mater.* **2016**, *6* (3), 1501449.
- (11) Wei, X.; Xu, W.; Vijayakumar, M.; Cosimbescu, L.; Liu, T.; Sprenkle, V.; Wang, W. TEMPO-based catholyte for high-energy density nonaqueous redox flow batteries. *Adv. Mater.* **2014**, *26* (45), 7649–7653.
- (12) Luo, J.; Hu, B.; Debruler, C.; Liu, T. L. A π -Conjugation Extended Viologen as a Two-Electron Storage Anolyte for Total Organic Aqueous Redox Flow Batteries. *Angew. Chem.* **2018**, *130* (1), 237–241.
- (13) Park, M.; Ryu, J.; Wang, W.; Cho, J. Material design and engineering of next-generation flow-battery technologies. *Nat. Rev. Mater.* **2017**, *2* (1), 16080.
- (14) Gerhardt, M. R.; Tong, L.; Gómez-Bombarelli, R.; Chen, Q.; Marshak, M. P.; Galvin, C. J.; Aspuru-Guzik, A.; Gordon, R. G.; Aziz, M. J. Anthraquinone Derivatives in Aqueous Flow Batteries. *Adv. Energy Mater.* **2017**, *7* (8), 1601488.
- (15) Huskinson, B. T.; Marshak, M.; Suh, C.; Er, S.; Gerhardt, M.; Galvin, C. J.; Chen, X.; Aspuru-Guzik, A.; Gordon, R. G.; Aziz, M. J. A metal-free organic–inorganic aqueous flow battery. *Nature* **2014**, *505*, 195.
- (16) Mukhopadhyay, A.; Hamel, J.; Katahira, R.; Zhu, H. Metal-free aqueous flow battery with novel ultrafiltered lignin from wood as electrolyte. *ACS Sustainable Chem. Eng.* **2018**, *6*, 5394.
- (17) Hollas, A.; Wei, X.; Murugesan, V.; Nie, Z.; Li, B.; Reed, D.; Liu, J.; Sprenkle, V.; Wang, W. A biomimetic high-capacity phenazine-based anolyte for aqueous organic redox flow batteries. *Nature Energy* **2018**, *3* (6), 508.
- (18) Hu, B.; Seefeldt, C.; DeBruler, C.; Liu, T. L. Boosting the energy efficiency and power performance of neutral aqueous organic redox flow batteries. *J. Mater. Chem. A* **2017**, *5* (42), 22137–22145.
- (19) Luo, J.; Hu, B.; Debruler, C.; Bi, Y.; Zhao, Y.; Yuan, B.; Hu, M.; Wu, W.; Liu, T. L. Unprecedented capacity and stability of ammonium ferrocyanide catholyte in pH neutral aqueous redox flow batteries. *Joule* **2019**, *3* (1), 149–163.
- (20) Luo, J.; Sam, A.; Hu, B.; DeBruler, C.; Wei, X.; Wang, W.; Liu, T. L. Unraveling pH dependent cycling stability of ferricyanide/ferrocyanide in redox flow batteries. *Nano Energy* **2017**, *42*, 215–221.
- (21) Janoschka, T.; Martin, N.; Martin, U.; Friebe, C.; Morgenstern, S.; Hiller, H.; Hager, M. D.; Schubert, U. S. An aqueous, polymer-based redox-flow battery using non-corrosive, safe, and low-cost materials. *Nature* **2015**, *527*, 78.
- (22) Carretero-González, J.; Castillo-Martínez, E.; Armand, M. Highly water-soluble three-redox state organic dyes as bifunctional analytes. *Energy Environ. Sci.* **2016**, *9* (11), 3521–3530.
- (23) Komboonchoo, S.; Bechtold, T. Natural dyeing of wool and hair with indigo carmine (CI Natural Blue 2), a renewable resource based blue dye. *J. Cleaner Prod.* **2009**, *17* (16), 1487–1493.
- (24) Holmes, S. T.; Dybowski, C. Carbon-13 chemical-shift tensors in indigo: A two-dimensional NMR-ROCSA and DFT Study. *Solid State Nucl. Magn. Reson.* **2015**, *72*, 90–95.
- (25) König, J. 2 - Food colour additives of synthetic origin A2. In *Colour Additives for Foods and Beverages*; Scotter, M. J., Ed.; Woodhead Publishing: Oxford, U.K., 2015; pp 35–60.
- (26) Harp, B. P.; Barrows, J. N. 4 - US regulation of color additives in foods A2. In *Colour Additives for Foods and Beverages*; Scotter, M. J., Ed.; Woodhead Publishing: Oxford, U.K., 2015; pp 75–88.
- (27) Vandenabeele, P.; Moens, L. Micro-Raman spectroscopy of natural and synthetic indigo samples. *Analyst* **2003**, *128* (2), 187–193.
- (28) Shadi, I. T.; Chowdhry, B. Z.; Snowden, M. J.; Withnall, R. Analysis of the conversion of indigo into indigo carmine dye using SERRS. *Chem. Commun.* **2004**, No. 12, 1436–1437.
- (29) Song, H. K.; Palmore, G. T. R. Redox-Active Polypyrrole: Toward Polymer-Based Batteries. *Adv. Mater.* **2006**, *18* (13), 1764–1768.
- (30) de Keijzer, M.; van Bommel, M. R.; Keijzer, R. H.-d.; Knaller, R.; Oberhumer, E. Indigo carmine: Understanding a problematic blue dye. *Stud. Conserv.* **2012**, *57* (sup1), S87–S95.
- (31) Komboonchoo, S.; Bechtold, T. Sorption characteristics of indigo carmine as a blue colorant for use in one-bath natural dyeing. *Text. Res. J.* **2010**, *80* (8), 734–743.
- (32) Barden, T. C. Indoles: Industrial, Agricultural and Over-the-Counter Uses. In *Heterocyclic Scaffolds II: Reactions and Applications of Indoles*; Gribble, G. W., Ed.; Springer: Berlin, 2010; pp 31–46.
- (33) Hamidi-Asl, E.; Raoof, J. B.; Ojani, R.; Hejazi, M. S. Indigo carmine as new label in PNA biosensor for detection of short sequence of p53 tumor suppressor gene. *Electroanalysis* **2013**, *25* (9), 2075–2083.
- (34) Moreno, M.; Ortiz-Sánchez, J. M.; Gelabert, R.; Lluch, J. M. A theoretical study of the photochemistry of indigo in its neutral and dianionic (leucoindigo) forms. *Phys. Chem. Chem. Phys.* **2013**, *15* (46), 20236–20246.
- (35) Solís Correa, H.; Ortiz, E.; Uc, V. H.; Barceló Quintal, I. D.; Hernández Avila, J. L. Indigo stability: an ab initio study. *Mol. Simul.* **2011**, *37* (13), 1085–1090.
- (36) Su, L.; Zhang, D.; Peng, S.; Wu, X.; Luo, Y.; He, G. Orientated graphene oxide/Nafion ultra-thin layer coated composite membranes for vanadium redox flow battery. *Int. J. Hydrogen Energy* **2017**, *42* (34), 21806–21816.
- (37) Yang, Z.; Tong, L.; Tabor, D. P.; Beh, E. S.; Goulet, M. A.; De Porcellinis, D.; Aspuru-Guzik, A.; Gordon, R. G.; Aziz, M. J. Alkaline Benzoinquinone Aqueous Flow Battery for Large-Scale Storage of Electrical Energy. *Adv. Energy Mater.* **2018**, *8* (8), 1702056.
- (38) Liu, T.; Wei, X.; Nie, Z.; Sprenkle, V.; Wang, W. A Total Organic Aqueous Redox Flow Battery Employing a Low Cost and Sustainable Methyl Viologen Anolyte and 4-HO-TEMPO Catholyte. *Adv. Energy Mater.* **2016**, *6* (3), 1501449.
- (39) Sevov, C. S.; Hickey, D. P.; Cook, M. E.; Robinson, S. G.; Barnett, S.; Minteer, S. D.; Sigman, M. S.; Sanford, M. S. Physical organic approach to persistent, cyclable, low-potential electrolytes for flow battery applications. *J. Am. Chem. Soc.* **2017**, *139* (8), 2924–2927.
- (40) Bentouami, A.; Ouali, M. S.; De Menorval, L.-C. Photocatalytic decolorization of indigo carmine on 1,10-phenanthroline intercalated bentonite under UV-B and solar irradiation. *J. Photochem. Photobiol., A* **2010**, *212*, 101–106.
- (41) Oh, K.; Weber, A. Z.; Ju, H. Study of bromine species crossover in H₂/Br₂ redox flow batteries. *Int. J. Hydrogen Energy* **2017**, *42* (6), 3753–3766.
- (42) Li, G.; Jia, Y.; Zhang, S.; Li, X.; Li, J.; Li, L. The crossover behavior of bromine species in the metal-free flow battery. *J. Appl. Electrochem.* **2017**, *47* (2), 261–272.
- (43) DeBruler, C.; Hu, B.; Moss, J.; Luo, J.; Liu, T. L. A sulfonate-functionalized viologen enabling neutral cation exchange, aqueous organic redox flow batteries toward renewable energy storage. *ACS Energy Letters* **2018**, *3* (3), 663–668.

(44) Hu, B.; DeBruler, C.; Rhodes, Z.; Liu, T. L. Long-cycling aqueous organic redox flow battery (AORFB) toward sustainable and safe energy storage. *J. Am. Chem. Soc.* **2017**, *139* (3), 1207–1214.

(45) Luo, J.; Hu, B.; Debruler, C.; Liu, T. L. A π -Conjugation Extended Viologen as a Two-Electron Storage Anolyte for Total Organic Aqueous Redox Flow Batteries. *Angew. Chem., Int. Ed.* **2018**, *57* (1), 231–235.

(46) Haynes, W. M. *CRC Handbook of Chemistry and Physics*, 96th ed.; CRC Press: Boca Raton, FL, June 9, 2015.

(47) Xiang, C.; Papadantonakis, K. M.; Lewis, N. S. Principles and implementations of electrolysis systems for water splitting. *Mater. Horiz.* **2016**, *3* (3), 169–173.

(48) Mukhopadhyay, A.; Yang, Y.; Li, Y.; Chen, Y.; Li, H.; Natan, A.; Liu, Y.; Cao, D.; Zhu, H. Mass Transfer and Reaction Kinetic Enhanced Electrode for High-Performance Aqueous Flow Batteries. *Adv. Funct. Mater.* **2019**, 1903192.

(49) Frisch, M. J.; Pople, J. A.; Binkley, J. S. Self-consistent molecular orbital methods 25. Supplementary functions for Gaussian basis sets. *J. Chem. Phys.* **1984**, *80* (7), 3265–3269.